ChemPlusChem

Research Article
doi.org/10.1002/cplu.202200036

Chemistry Europe
European Chemical Societies Publishing

www.chempluschem.org

Promising Electrocatalytic Water and Methanol Oxidation Reaction Activity by Nickel Doped Hematite/Surface Oxidized Carbon Nanotubes Composite Structures

Bibhudatta Malik[+],[a] Sumit Majumder[+],[a] Roberto Lorenzi,[b] Ilana Perelshtein,[a] Michal Ejgenberg,[a] Alberto Paleari,[b] and Gilbert Daniel Nessim*[a]

Tailoring the precise construction of non-precious metals and carbon-based heterogeneous catalysts for electrochemical oxygen evolution reaction (OER) and methanol oxidation reaction (MOR) is crucial for energy conversion applications. Herein, this work reports the composite of Ni doped Fe_2O_3 (Ni–Fe_2O_3) with mildly oxidized multi-walled CNT (O–CNT) as an outstanding Mott-Schottky catalyst for OER and MOR. O–CNT acts as a co-catalyst which effectively regulates the charge transfer in Ni–Fe_2O_3 and thus enhances the electrocatalytic performance. Ni–Fe_2O_3/O–CNT exhibits a low onset potential of 260 mV and overpotential 310 mV @ 10 mA cm^{-2} for oxygen evolution. Being a Mott-Schottky catalyst, it achieves the higher flat band potential of −1.15 V with the carrier density of 0.173×10^{24} cm^{-3}. Further, in presence of 1 M CH_3OH, it delivers the MOR current density of 10 mA cm^{-2} at 1.46 V vs. RHE. The excellent electrocatalytic OER and MOR activity of Ni–Fe_2O_3/O–CNT could be attributed to the synergistic interaction between Ni-doped Fe_2O_3 and O–CNT.

Introduction

The current energy scenario and global energy prerequisite is in need of high powered energy conversion devices such as the electrolyser system for green hydrogen generation.[1–3] Beneficially, hydrogen provides CO_2 emission free, efficient, and economical energy production options in contrast to the non-renewable energy sectors.[4–6] At the present time, around 90 percent of the hydrogen in the world is produced via coal gasification and steam reforming methods.[7] Although these methods of H_2 production fully fill our demand, but are not ecofriendly and cause vast pollution.[8] H_2 generation using electrochemical water splitting can be an efficient expertise for the next generation energy technology. However, the efficiency of H_2 production is affected by the sluggish kinetics of anodic oxygen evolution reaction (OER), a half cell reaction of overall water splitting. The enormous potential loss for OER, owing to the complex four electron transfer process (4e$^-$), is a main barrier to the grid scale production of hydrogen.[9–13] Hence, efficient catalysts are desired which can lower the overpotential and boost the production rate of molecular hydrogen. Noble metal-based OER electrocatalysts, such as IrO_2 and RuO_2, are the best opt for such application.[14–17] However, their high cost and low availability in the earths' crust restricts them for further use.[18,19] Plenty of studies have been devoted to noble metal free transition metal-based systems to gain high output. The examined systems include first row transition metal such as Ni, Co, Fe, Cu and Mn based oxides, hydroxides, phosphides, chalcogenides, borides, etc.[20–30] Some which render excellent performance and some show comparable activity with noble metals. In order to deal with the current energy demand, finding more efficient catalysts are highly urgent.

In another strategy, to solve the energy scarcity issues specifically, direct alcohol fuel cells are rooted as potential energy platform which can convert the chemical energy available in alcohol to electrical energy.[31,32] Based on this, promising technologies such as direct liquid fuel cells (DLFCs) with greater efficiency could be established, owing to their high-power density and easy transport and storage qualities.[33] Moreover, methanol is inexpensive, readily available, biodegradable, and shows decent electrochemical behavior. Methanol oxidation reaction (MOR) is an anodic half reaction which converts chemical energy to electricity in alkaline media as given below:

$$CH_3OH + 6OH^- \rightarrow CO_2 + 5H_2O + 6e^-,$$
$$E^o = -0.81 \text{ V vs. NHE } (pH = 14)$$

Basically, platinum (Pt) and its alloys with both other noble and non-noble metals demonstrate excellent MOR activity.[34–37] But the high price and CO poisoning restrict the commercialization of Pt systems in direct methanol fuel cells.[38,39] The majority

[a] B. Malik,[+] Dr. S. Majumder,[+] Dr. I. Perelshtein, Dr. M. Ejgenberg, Prof. G. D. Nessim
Department of Chemistry and Institute of Nanotechnology
Bar-Ilan University
Ramat Gan 52900 (Israel)
E-mail: gdnessim@biu.ac.il
[b] Dr. R. Lorenzi, Prof. A. Paleari
Department of Materials Science
University of Milano-Bicocca
Via R. Cozzi 55, 20125 Milano (Italy)
[+] These authors contributed equally to this manuscript.

Supporting information for this article is available on the WWW under https://doi.org/10.1002/cplu.202200036

of studies for catalyzing MOR have been used by noble metal based systems where, the detected products are mainly CO_2 and H_2O, and the research is restricted to understanding further the selective electro-oxidation of products of methanol. Formic acid, one of the widely used chemicals in many industries (traded with high price), can be obtained from the partial oxidation of methanol.[40,41] Thus, development of cheaper and high performance electrocatalysts are required to enhance the rate of selective electro-oxidation of methanol to produce HCOOH.

Moreover, recent reports reveal that coupling hematite (Fe_2O_3) with other metal oxides, with Pt and doping of other transition metals to hematite, delivers a much better electrocatalytic performance.[42–45] Fe_2O_3 and other transition metal oxides exhibit poor bifunctional electrocatalytic activity owing to their inferior electrical conductivity. Zhong et al. used an effective approach where they coupled the nitrogen-doped carbon sheets with Co/CoOx heterojunctions to obtain optimal electrocatalytic activity, where the hybrid enables the faster charge and mass transport.[46] Zhong et al. further observed a very promising ORR electrocatalytic activity, by hybridizing carbon hollow spheres with Co/NC systems.[47] In an another research, Feng et al. effectively regulated the hetero-interfaces of bimetallic nanoparticles with N-doped porous carbon and MoS_2, and obtained very high HER electrocatalytic performance.[48] Thus, inspired by these researches, we coupled surface-oxidized CNT with Ni doped Fe_2O_3 as a bi-functional electrocatalyst for OER and MOR. O–CNT here acts as a co-catalyst and provides good conductive support to Ni–Fe_2O_3, due to presence of oxygen containing groups, particularly C=O. The keto group, C=O, alters the electronic properties of the adjacent carbon atoms and facilitates the electrocatalytic oxidation process.[49]

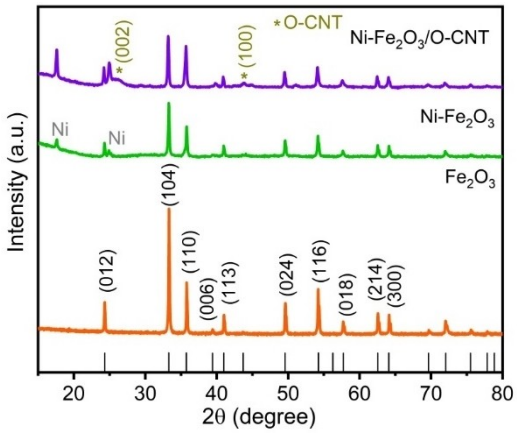

Figure 1. XRD patterns of the as-prepared materials.

Results and Discussions

The synthesis procedure of the obtained catalyst has been sketched and provided below in Scheme 1 for understanding of the process and parameters.

The phase clarity and crystallinity of the prepared materials were validated by X-ray diffraction (XRD), as shown in Figure 1. The formation of α-Fe_2O_3 is confirmed due to the presence of diffraction peaks at 24.1, 33, 35.6, 40.8, 49.4 and 54° etc. which is in well agreement with the reference code: **00-013-0534**. The reference code: **00-013-0534** represents the diffraction standard card for Hematite with the empirical formula of Fe_2O_3 which belongs to the Rhombohedral crystal system and space group of R-3c. After the doping of Ni^{2+}, we identified two more new peaks that are present at 2θ of 17.7° and 24.8°. Likewise, Yin et al. observed a few less intense diffraction peaks upon the doping of transition metals (Mn, Ni, Co, Zn etc) in Fe_2O_3. Moreover, the obtained peaks owing to Ni^{2+} doping which do

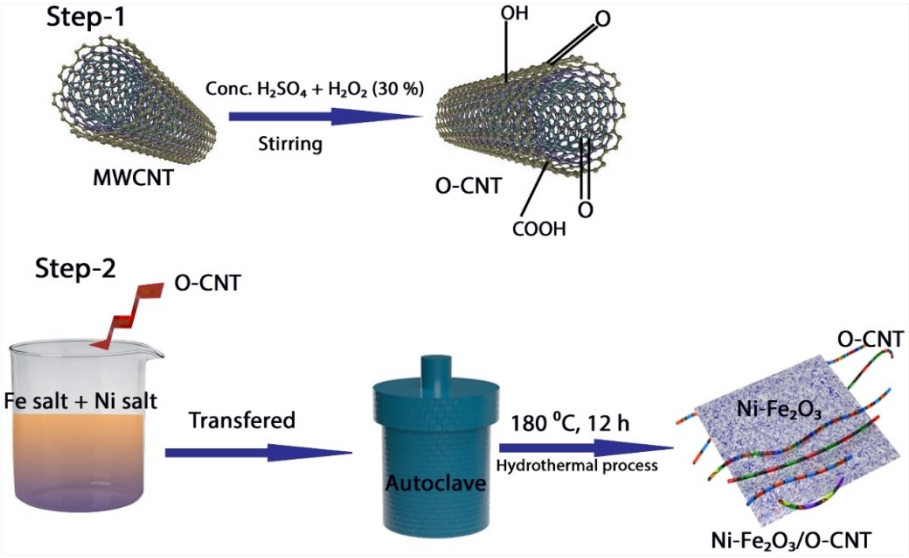

Scheme 1. Synthesis process of Ni–Fe_2O_3/O–CNT.

not match with the metallic either Ni or $Ni(OH)_2$ and NiO. Also, the enhancement of peak intensity at 2θ of 17.7° and 24.8° in case of Ni–Fe_2O_3/O–CNT as compared to Ni–Fe_2O_3 that is observed, could be due to the more ordering and crystallinity of the structure in presence of oxidized CNT. Similarly, in Ni–Fe_2O_3/O–CNT, two more broad diffraction peaks at 26.4° and 43.5° corresponding to (002) and (100) planes of carbon nanotube, respectively, confirm the existence of oxidized CNT.

Raman spectra of Fe_2O_3, O–CNT, and O–CNT_Fe_2O_3 composite are reported in Figure 2, along with the Ni doped samples. Iron oxide peaks confirm the results obtained by XRD and are attributable to Fe_2O_3 in the hematite phase. Its corundum-type crystalline structure belongs to the D_{3d}^6 group for which seven Raman-active modes ($2A_{1g}+5E_g$) and six IR-active modes ($4E_u+2A_{2u}$) are expected from symmetry considerations.[50] Namely, the peaks in the lower wavenumber region of the Raman spectra at 224, 242, 290, 406, 487, 606 cm^{-1} correspond to $A_{1g}(1)$, $E_g(1)$, unresolved[51] $E_g(2)+E_g(3)$, $E_g(4)$, $A_{1g}(2)$, and $E_g(5)$ Raman modes,[52] respectively. Besides these peaks', other spectral features in the higher wavenumber region can be seen: peaks at 655 and 808 cm^{-1} and a series of bands in the range

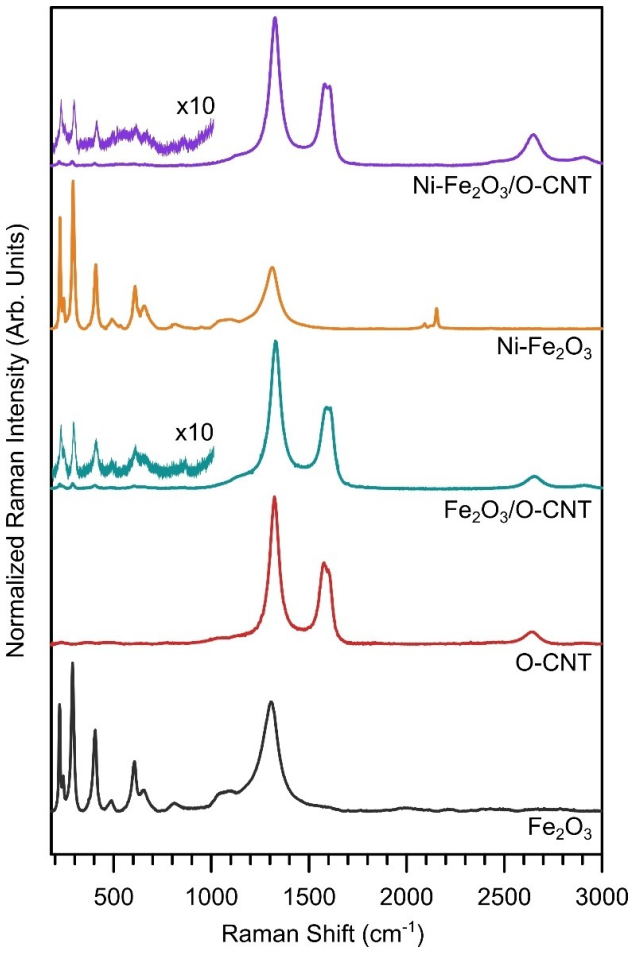

Figure 2. Normalized Raman spectra of Fe_2O_3 (black line), O–CNT (red line), Fe_2O_3/O–CNT (teal blue line), Ni–Fe_2O_3 (orange line), and Ni–Fe_2O_3/O–CNT (violet line) samples. Raman spectra of Fe_2O_3/O–CNT and Ni–Fe_2O_3/O–CNT are also shown with a magnification factor x10 in the range 180–950 cm^{-1}. Spectra are vertical shifted for clarity.

950–1700 cm^{-1} with the most prominent peak centred at 1310 cm^{-1}. Their intensities strongly depend on the excitation wavelength, suggesting the occurrence of resonance effect. The 633 nm He–Ne laser line, used in the present setup, actually falls very close to the optical absorption edge of Fe_2O_3, leading to Raman enhancement.[53] This condition makes possible the detection of symmetry-forbidden transitions such as the 655 cm^{-1} E_u(LO) peak and its overtone at 1310 cm^{-1} (2LO). The origin of the latter peak has been disputed and early works pointed to a spin-wave related origin. In fact, at room temperature, hematite is a canted antiferromagnet[54] and collective excitation of electron spin can take place, giving rise to the so-called optical active magnons. However, several studies gave clear-cut evidence about the correct interpretation of the high wavenumber region in the Raman spectra of hematite.[55,56] In particular, magnon modes are located at 790 cm^{-1} (1 magnon) and 1587 cm^{-1} (2 magnon, not detected in our experiment), while symmetry forbidden modes appear at 657 cm^{-1} (LO) and 1323 cm^{-1} (2LO). Remarkably, the intensity of these modes varies according to the experimental setup used in Raman acquisition – excitation wavelength, tip, and surface enhancement – and material morphology. As regarding this aspect, it has been shown that the possibility of detecting *ungerade* IR-active modes in Raman spectra of α-Fe_2O_3 is greater in those samples which facilitate breakdown of centrosymmetry[57,58] such as the presence of surface defects, amorphization, and large surface/volume ratio as in the present synthesis where highly branched systems were produced. Raman spectra of O–CNT, in accordance with literature,[59] shows three main features: the D band at about 1350 cm^{-1}, the G band at 1585 cm^{-1}, and the G' or 2D band at 2700 cm^{-1}. The D peak is due to defect-related scattering such as finite graphitic sheets, vacancies, and heteroatoms; the graphitic G band is typical of the C–C bond in sp^2 configuration; and the G' band is an overtone of the D band. As expected in MWCNT, the G band splits in two sub bands: the G^+ peak at 1590 cm^{-1}, due to in-plane vibrations along the tube axis, and the G^- peak at 1570 cm^{-1}, due to in-plane vibrations along the circumferential direction. In the O–CNT Raman spectra no other features are registered. In particular, the absence of radial breathing modes below 350 cm^{-1} suggests that the diameters of the MWCNTs are greater than 2 nm, in accordance with HR-TEM analysis. The spectrum of the composite material O–CNT/Fe_2O_3 is a superposition of the parent spectra with a dominance of O–CNT signals, confirming the successful synthesis of composite. The addition of Ni does not introduce significant variation to the Raman spectra, expecting a small peak at 2555 cm^{-1} in the Ni–Fe_2O_3 spectrum, which is attributable to minor cyanide residue used during the synthesis.[60]

Microstructure analysis of Ni–Fe_2O_3/O–CNT were carried out using electron microscopic techniques. Both the low- and high-resolution scanning electron microscopy images suggest that sheets of Ni–Fe_2O_3 sheets are wrapped with the oxidized CNTs, as shown in Figure S1a and S1b. The low and high-resolution transmission electron microscopy, TEM and HR-TEM images as shown in Figure 3a and 3b supports the SEM results and confirms that the O–CNTs are well coupled with the sheets of

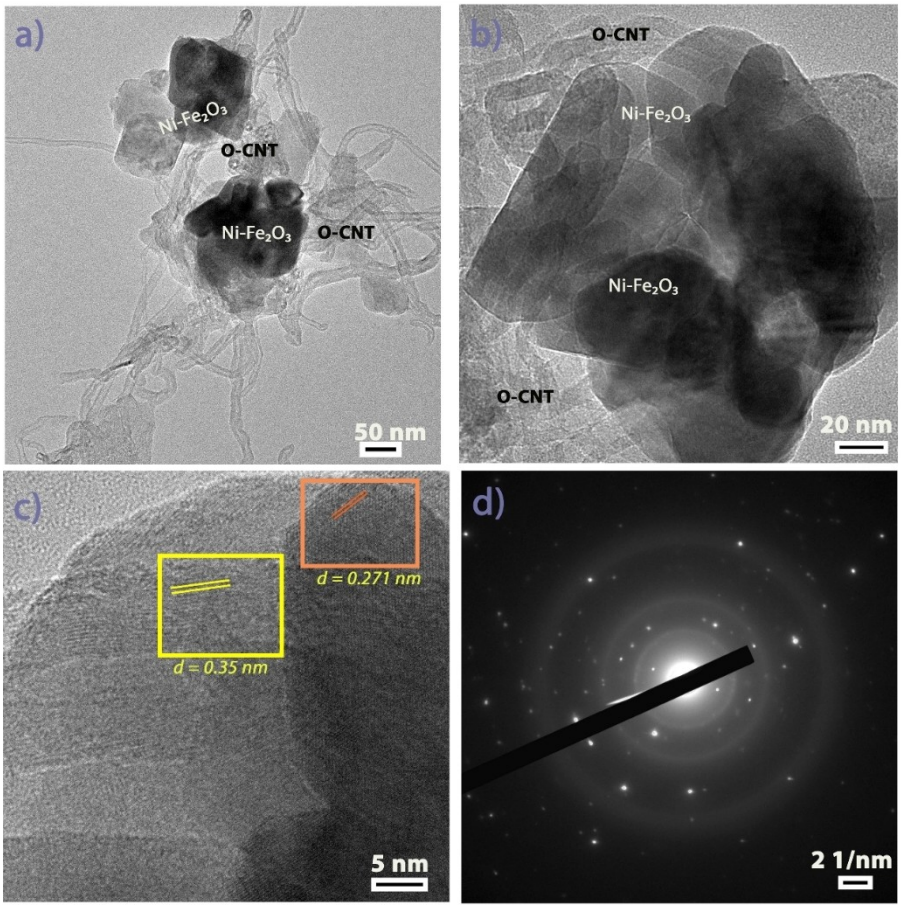

Figure 3. Low and high magnification TEM images of Ni–Fe_2O_3/O–CNT in a) and b) respectively c) lattice fringes and d) SAED pattern.

Ni–Fe_2O_3. The measured lattice distances, *d*-spacings of 0.35 nm and 0.271 nm belong to the (002) and (104) planes of O–CNT and Fe_2O_3, respectively, as depicted in Figure 3c. The crystallinity nature of Ni–Fe_2O_3/O–CNT is further verified using selected area electron diffraction (SAED) pattern. Figure 3d reveals that the formed hybrid structure is Ni–Fe_2O_3/O–CNT polycrystalline by nature, which supports XRD. It can be noticed from Figure 3d that the SAED pattern is comprised of incomplete rings, which indicates that the particles exhibit random crystallographic orientations. The energy dispersive spectroscopy (EDS) spectrum in Figure S1 clarifies the presence of Fe, Ni, C and O.

Further, the scanning transmission electron microscopy-energy dispersive spectroscopy (STEM-EDS) mapping elucidates the distribution of four elements (Figure 4a). The color mapping images reveal the existence of elements such as Fe, Ni, C and O (From Figure 4b–e). Its shows that CNTs are everywhere and covered the equally distributed Fe and O. Further, it is clear that the concentration of Ni is very low, which are distributed over Fe.

Elemental composition and chemicals state of the elements have been verified by X-ray photoelectron spectroscopy (XPS). Core level Fe 2p spectrum can be split into $2p_{3/2}$ and $2p_{1/2}$ as shown in Figure 5a. The principal peak situated at 711 eV reveals that iron exists in the Fe^{+3} state, the main peak of Fe $2p_{1/2}$ is located at 725.2 eV, while other satellite peaks appear at the binding energies of 713 eV, 719.8 eV and 734.5 eV. In case of Ni $2p_{3/2}$, the main peak present at 856.5 eV belongs to Ni^{2+}, while other peak positions at 858 eV and 863.4 eV are ascribed to the satellite peak (Figure 5b). High resolution spectrum of C 1s in Figure 5c demonstrates that peaks present at 284.9 eV, 285.9 eV, 287.2 eV, 289.8 eV and 291.7 eV belong to the sp^2 carbon (C=C), hydroxyl/epoxy (C-OH/C–O–C), C=O group, carboxyl group (-COOH) and π–π^* transition. The deconvoluted spectrum of O 1s (Figure 5d) at 530.2 eV, 532.8 eV and 534.6 eV are belonging to Fe–O bonding, Fe-OH and Fe-H_2O. We compared the XPS spectra of pristine Fe_2O_3 with Ni–Fe_2O_3 to notice the change in spectrum behavior. Figure S9 suggests that owing to the doping of Ni, the original position of Fe $2p_{3/2}$ has been shifted to 711. 2 eV from 710.4 eV, which are corresponds to the Fe^{3+} state. The main peaks of Fe (III) in cases of Fe_2O_3 with Ni–Fe_2O_3 are located at 710.5 and 711 eV, respectively. This forward shifting of peak is observed due to the introduction Ni^{2+} into the lattice of hematite, which might have significant impact on the electronic structure of Fe_2O_3 which could be further explained by using EPR in the later section.

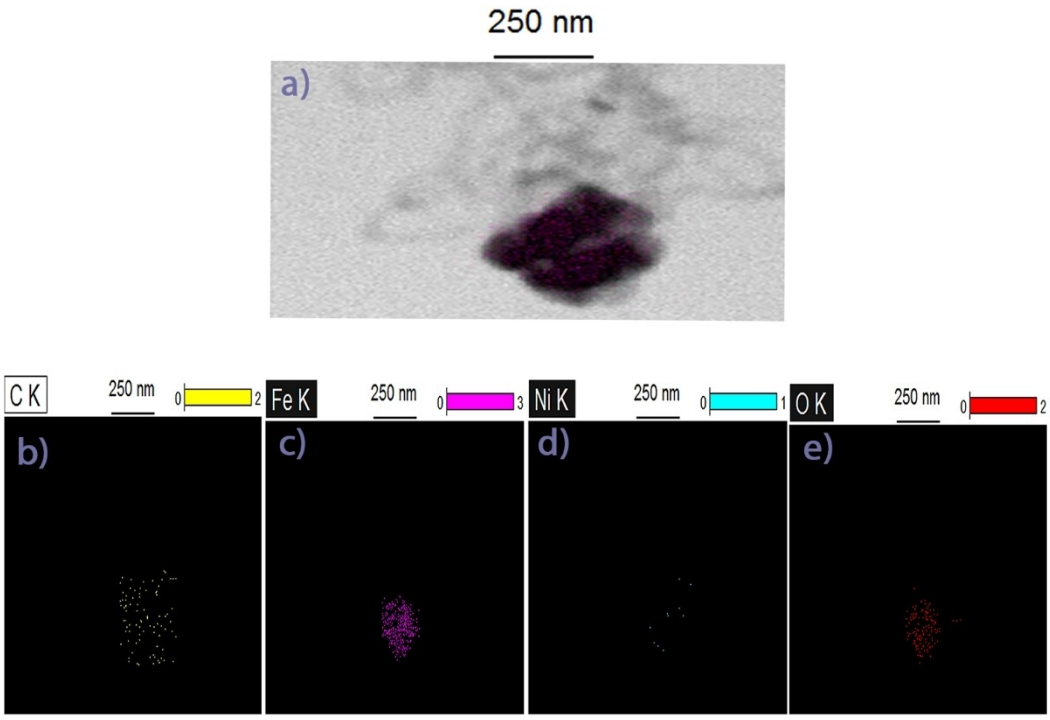

Figure 4. a) STEM color mapping images showing the distribution of distribution profiles for b) Carbon, c) Iron, d) Nickel and e) Oxygen.

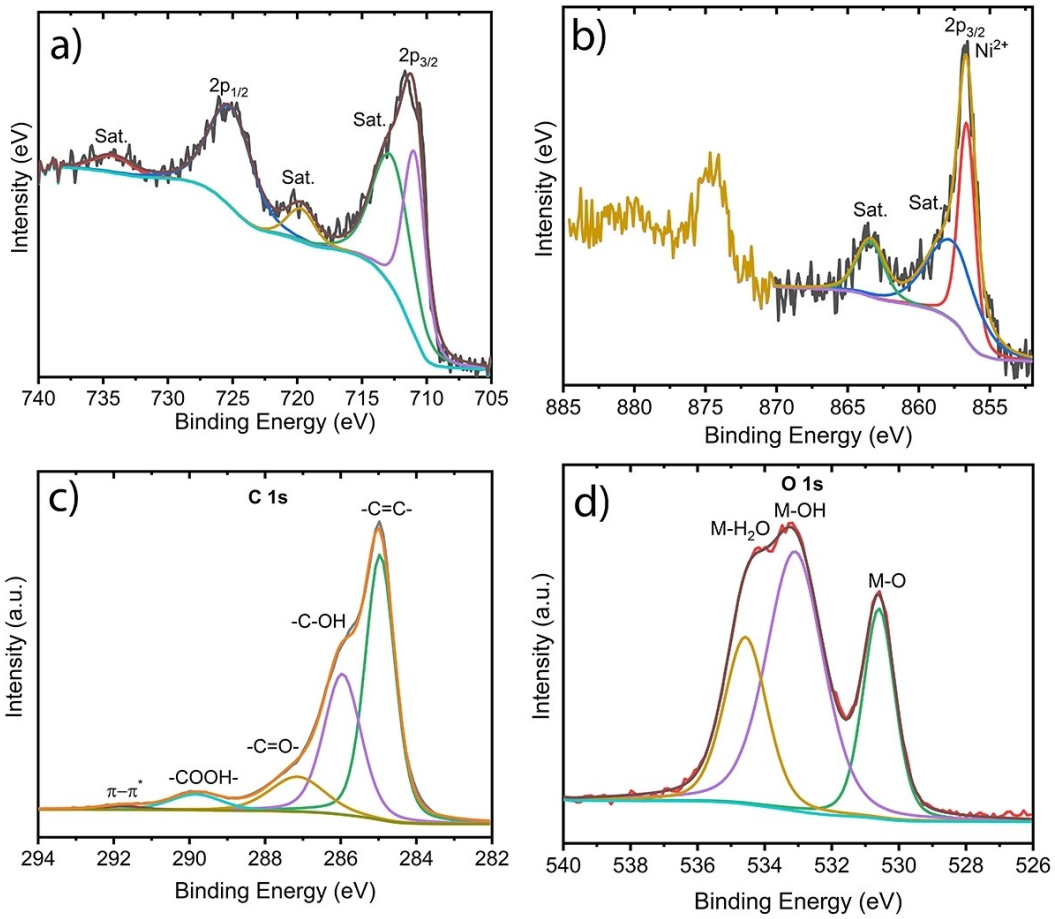

Figure 5. XPS spectrum of a) Fe 2p, b) Ni 2p, c) C 1s and d) O 1s spectrum.

We carried out the electron paramagnetic resonance (EPR) at room temperature (Figure 6) in order to gain some fruitful knowledge about the electronic environment of Fe_2O_3 and the effect of Ni doping to it which has direct relationship with the electrocatalytic activity. In case of Fe_2O_3, where iron exists in the Fe^{3+} state corresponds to d^5 configuration shows the EPR signals at $g \approx 5.8$–6.3 in the applied field, ΔHapp of 1690–1980 Gauss.[61] Usually, a g value greater than 2.001 is obtained due to presence of certain symmetry elements.[62] The resonance signal at $g \approx 5.8$ arises due to spin-spin coupling, $S = \pm 3/2$. EPR signal at around g value of 6.0 is attributed to the isolated Fe^{3+} ions (d^5 system) positioned in axially low-symmetry distorted sites.[62] Ni^{2+} (d^8) belongs to octahedral symmetry configuration with two unpaired electrons and thus it is EPR active. The Ni^{2+} doped with Fe_2O_3 exhibits resonance signal at 2.55–3.2 in the corresponding ΔHapp (G) = 2952–1880. The obtained broad resonance signal at $g \approx 2.55$ after Ni^{2+} incorporation confirms the alteration of local electronic environment of Fe_2O_3.

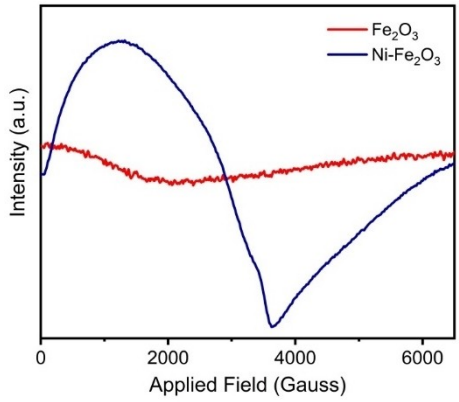

Figure 6. EPR spectra of the as-prepared materials.

Oxygen evolution performance: We have studied the electrocatalytic oxygen evolution performances of the prepared materials in an alkaline electrolyte (1 M KOH, pH = 14). The linear sweep voltammetry (LSV) data (Figure 7a) shows that bare Fe_2O_3 renders very high overpotential which is even larger than O–CNT. Fe_2O_3/O–CNT and Ni–Fe_2O_3 show the overpotential (η) of 450 mV and 360 mV at the current density of 10 mA cm^{-2}. Among all of them, Ni–Fe_2O_3/O–CNT exhibits the highest activity as compared to Ni–Fe_2O_3 and O–CNT. Ni–Fe_2O_3/O–CNT demonstrates a low onset potential of 260 mV and η_{10} of 310 mV which is 50 mV lower than Ni-doped hematite. Kinetics study is carried out using Tafel equation, $\eta = a + blogj$ (a and b are constants, and j is the current density). Tafel plots in Figure 7b indicate that Ni–Fe_2O_3/O–CNT demonstrates a smaller Tafel slope of 65 mV dec^{-1} as compared to Ni–Fe_2O_3 (71 mV dec^{-1}) and Fe_2O_3/O–CNT (80 mV dec^{-1}). Ni–Fe_2O_3/O–CNT experiences a negligible potential loss after 1000 cycles which proves the excellent durable nature of the material (Figure 7c).

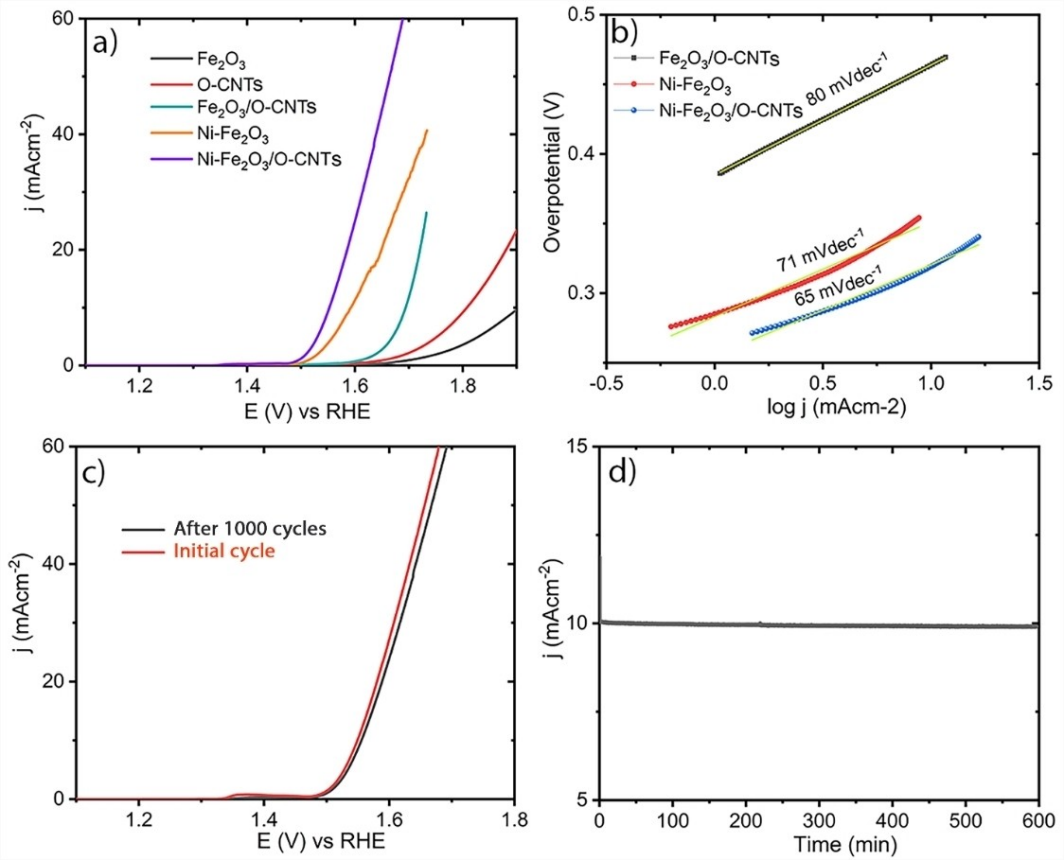

Figure 7. Comparative LSV of the prepared materials carried out 5 mVs^{-1}, b) comparative Tafel plots, c) durability test result of Ni–Fe_2O_3/O–CNT d) chronoamperometry (CA) study of Ni–Fe_2O_3/O–CNT.

To elucidate the stability of Ni–Fe_2O_3/O–CNT, we applied a constant potential of 1.54 V vs. RHE (j = 10 mA cm^{-2}). The chronoamperometry (CA) test result illustrates that the material is perfectly stable up to 10 h (Figure 7d).

To illuminate the reason behind the high OER activity of the Ni doped samples, we assessed the electrochemical active surface area (ECSA) of both Ni–Fe_2O_3 and Ni–Fe_2O_3/O–CNT. Figure 8a and 8b display the cyclic voltammograms (CVs) of Ni–Fe_2O_3 and Ni–Fe_2O_3/O–CNT in the non-faradic regions from where we calculated the electrical double layer capacitance (C_{DL}). Ni–Fe_2O_3/O–CNT and Ni–Fe_2O_3 show the C_{DL} of 0.413 and 0.29 mF cm^{-2}, respectively (Figure 8c). We estimated the ECSA using the formula, ECSA=C_{DL}/Cs where Cs is the capacitance of a smooth planar electrode (Cs = 0.04 mF cm^{-2}). Ni–Fe_2O_3/O–CNT and Ni–Fe_2O_3 exhibits the ECSA of 10.3 and 7.25 mF cm^{-2}. Larger ECSA proves the better activity shown by Ni–Fe_2O_3/O–CNT. The electrochemical impedance spectroscopy (EIS) probes into the mechanism which is studied in faradic regions and shows that both the materials catalyze OER via charge transfer process with the absence of any diffusion phenomena. Ni–Fe_2O_3/O–CNT displays faster charge transfer process than that of Ni–Fe_2O_3. Moreover, Ni–Fe_2O_3/O–CNT possesses better conductivity than Ni–Fe_2O_3 due to smaller curve (Figure 8d).

We then carried out the Mott-Schottky (MS) analysis to examine the charge transfer properties. We analyzed it by examining the EIS at 1kz with a small, perturbed AC amplitude of 10 mV as shown in Figure 9a. Figure 9b shows the MS plot of Ni–Fe_2O_3/O–CNT which we demonstrated separately due to lower intensity than Fe_2O_3 and Ni–Fe_2O_3. Fe_2O_3 shows a flat band potential of −0.914 7 V and a donor density of 6.008×10^{20} cm^{-3}, after doping with Ni it exhibits flat band potential and donor density of −1.101 V and 4.41×10^{20} cm^{-3}, respectively. The composite, Ni–Fe_2O_3/O–CNT shows much better flat band potential and donor density of −1.15 V and 0.173×10^{24} cm^{-3}, respectively.

Methanol electro-oxidation performance: We carried out the electro methanol oxidation reaction study in both 0.5 M and 1 M CH_3OH containing 1 M KOH (pH 14). Figure S3 shows the electrochemical behavior of O–CNT and Fe_2O_3 with the presence of 0.5 M methanol, which reveals that these materials are far from exhibiting the impressive activity. The cyclic voltammogram (CV) results in 0.5 M CH_3OH show that Ni–Fe_2O_3/O–CNT oxidizes methanol at early potential of 1.41 V vs. RHE and reaches the current density 10 mA cm^{-2} at 1.50 V vs. RHE. While the MOR for Ni–Fe_2O_3 and Fe_2O_3/O–CNT begin very lately as depicted in Figure 10a. In 1 M CH_3OH, Ni–Fe_2O_3/O–CNT shows the onset potential of 1.39 V and achieves 10 mA cm^{-2} at 1.46 V vs. RHE. Compared to the activity in 0.5 M CH_3OH, it shows better activity in 1 M CH_3OH, where the $j_{10\,mA\,cm^{-2}}$ difference is 40 mV (Figure 10c). Figure 10d suggests that it shows promising durability even after 2000 cycles.

The chronoamperometry (CA) test is carried out in 1 M methanol at 1.46 V vs. RHE, which is used to determine the methanol oxidation stability of Ni–Fe_2O_3/O–CNT. Figure 11a

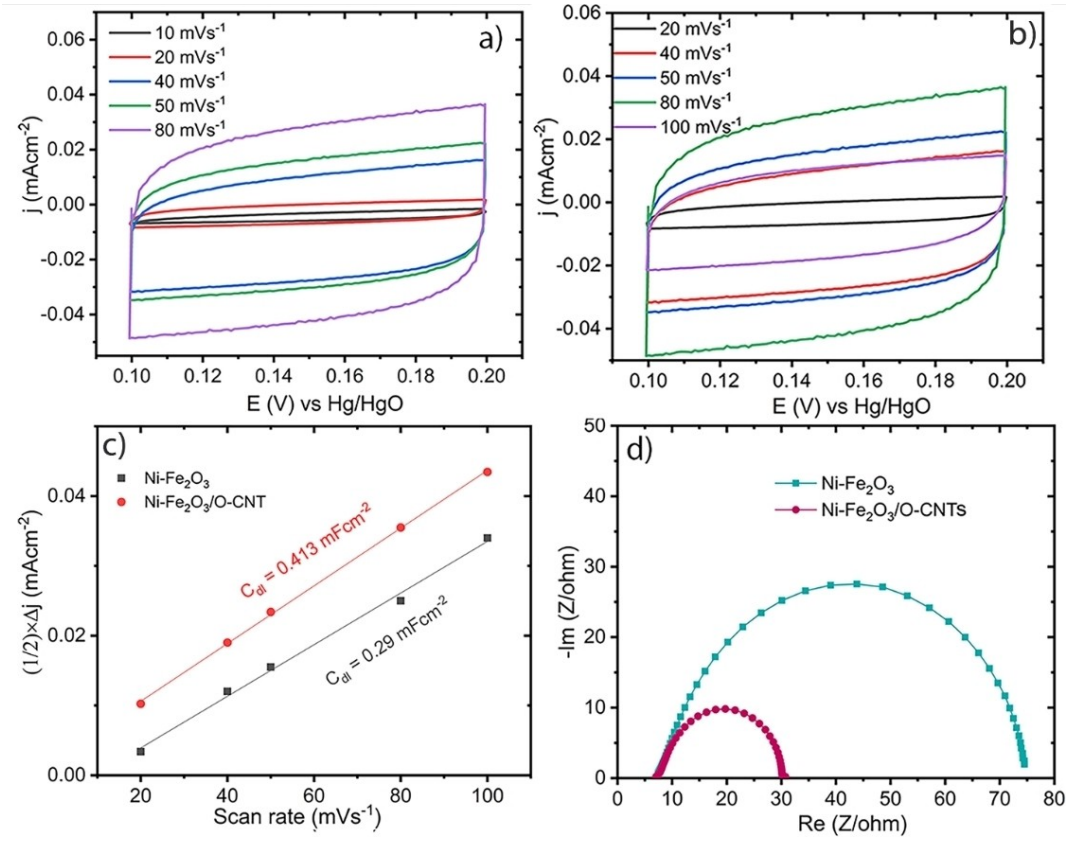

Figure 8. CVs of a) Ni–Fe_2O_3 and b) Ni–Fe_2O_3/O–CNT c) double layer capacitance plots and d) EIS plot.

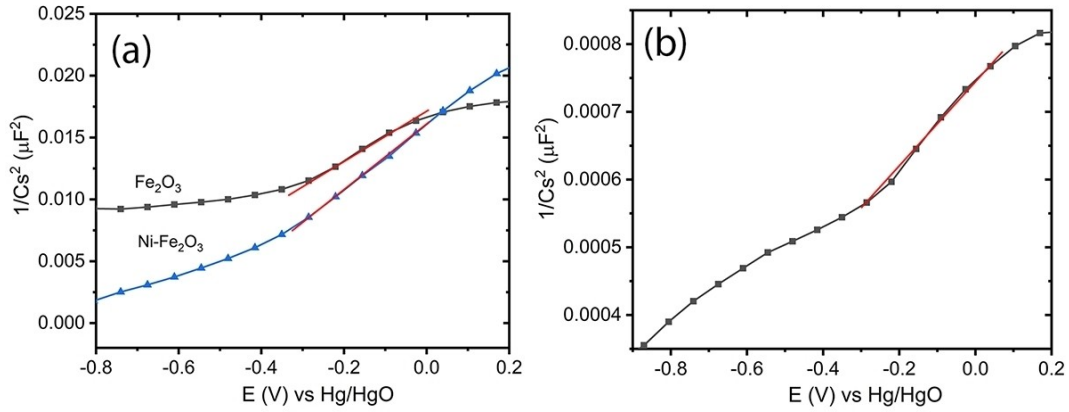

Figure 9. a) comparative MS plots b) MS plot of Ni–Fe_2O_3/O–CNT.

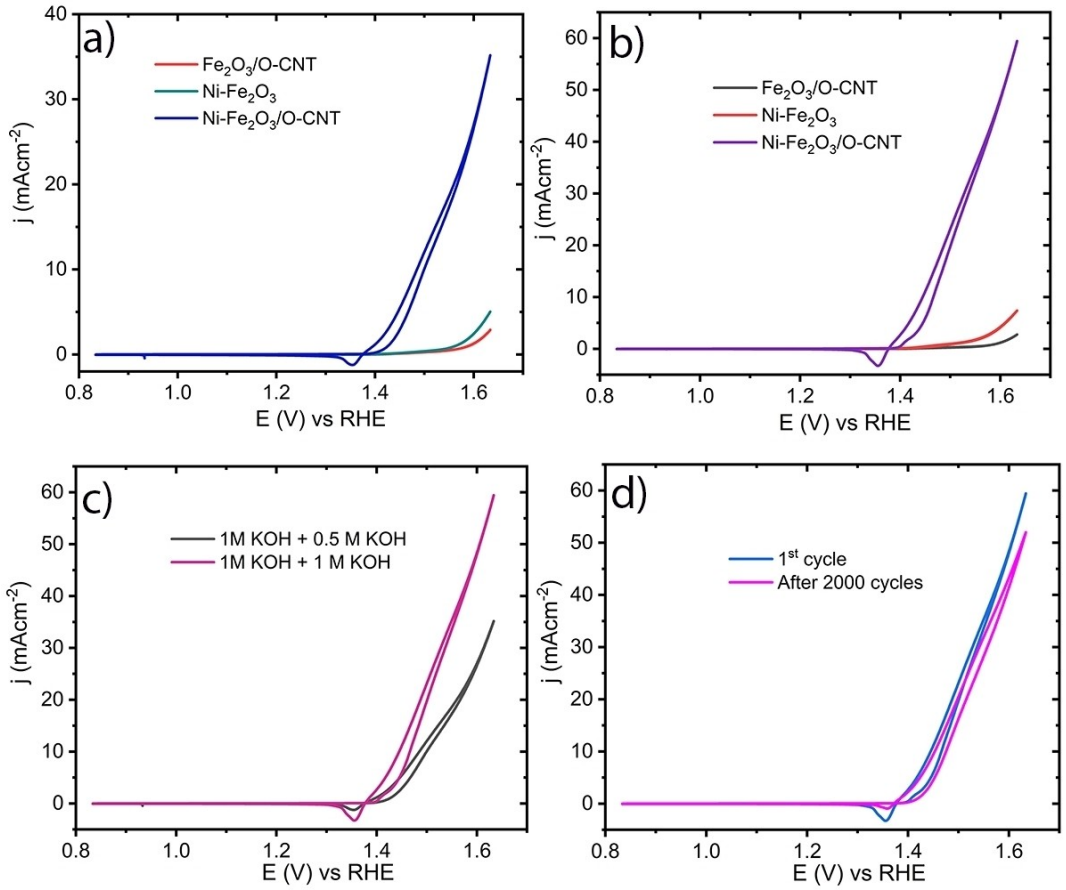

Figure 10. CVs of all three catalysts in presence of a) 0.5 M methanol b) 1 M methanol c) comparative CVs of Ni–Fe_2O_3/O–CNT in 0.5 and 1 M methanol d) durability test.

shows that Ni–Fe_2O_3/O–CNT possesses excellent stability as the current density drop is negligible and it is stable up to 500 minutes. Further, to understand the reaction process, we studied the electrochemical impedance (EIS) at the faradic potentials of the three catalysts. The Nyquist plots reveal that in presence of 1 M methanol, O–CNT/Fe_2O_3, Ni–Fe_2O_3 and Ni–Fe_2O_3/O–CNT possess curves, which is an indication of charge transfer process (Figure 11b). However, the diameter of the curves is much bigger for Fe_2O_3/O–CNT, Ni–Fe_2O_3, than the composite due to slower charge transfer processes. Furthermore, the inset stands for the Nyquist plot belonging to composite, Ni–Fe_2O_3/O–CNT, which is much smaller than the other two materials as the electronic conductivity after coupling is greatly enhanced. The Nyquist plot further confirms that the MOR proceeds via charge transfer process with the absence of mass transfer process.

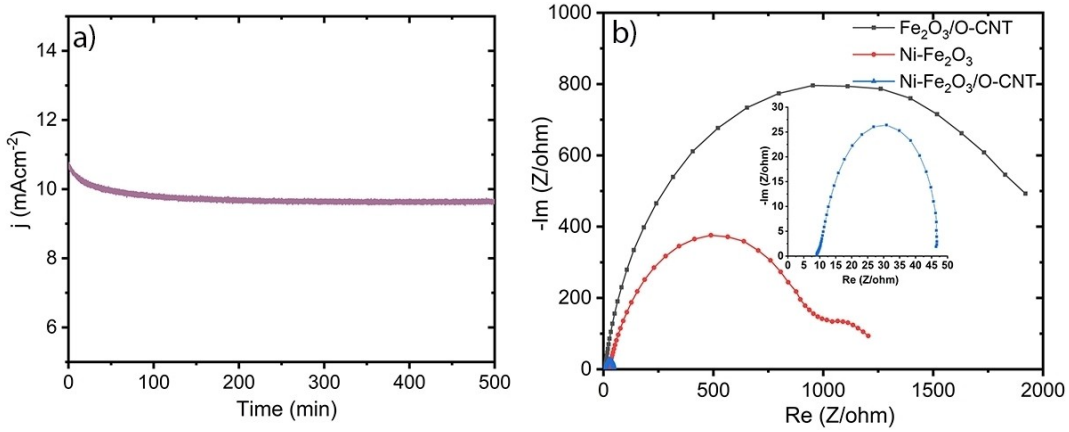

Figure 11. a) CA test result b) Nyquist plots of the prepared materials.

Postmortem analysis: It is well known that transition metal-based systems undergo transformation to metal(oxy)hydroxides during OER in an alkaline medium. We studied the structural and morphological changes of Ni–Fe_2O_3/O–CNT using microscopic and XPS analysis, after the 2000 CV cycles of OER and MOR. After OER, the slight change in morphology with the formation of pores on the Ni–Fe_2O_3 sheets is observed by TEM analysis (Figure S4a). The HR-TEM image in Figure S4b shows that Ni–Fe_2O_3 lost the crystallinity with the absence of fringes, while O–CNT exhibits the fringes. The EDS analysis confirms the existence of Fe, Ni, C and O (Figure S4c). Again, the TEM image of post MOR sample reveals that the morphology of the composite has been damaged (Figure S5a). Similar to the post OER sample as shown in Figure S4, the post MOR Ni–Fe_2O_3 in composite lost the crystallinity feature while O–CNT retains its crystallinity. The EDS validates the presence of Fe, Ni, C and O. And the presence of K is detected by EDS which most probably originated from the interaction between electrode and electrolyte (1 M KOH) (Figure 5c) (Same comment). Furthermore, we carried out the postmortem XPS analysis of the samples after both the oxidation process such as OER and MOR as given in Supporting Information. After prolonged cycling of OER, the main peak of Fe $2p_{3/2}$ is positively shifted to 711.7 eV which is again belongs to Fe^{+3} additionally, one more peak at lower binding energy (at 707.5 eV) is observed which can be assigned to $Fe^{+\delta}$ ($+\delta$ stands for small positive charge, close to zero valence) (Figure S6a). The principal peak position of Ni $2p_{3/2}$ belongs to Ni^{2+} also shifted to 856.8 eV as shown in Figure S6b. C 1s spectrum in (Figure S6c) reveal that some of the C=C bond broken into C–C and C=O has been completely disappeared. And the presence of peaks at 532.1 eV and 533.6 eV of O 1s spectrum suggest that it contains M–OH and M–H_2O bonding as provided in Figure S6d. After MOR, we observed the same valence state of Fe from Figure S7a likewise after OER which is Fe^{+3} as the principal peak of Fe $2p_{3/2}$ is found at 711.2 eV. The chemical state of Ni remains unchanged as compared to the fresh even after MOR. The main peak of Ni $2p_{3/2}$ as given in Figure S7b is located at 856. 4 eV which is designated to Ni^{+2}. The fitted O 1s spectrum confirms the presence of M–OH and M–H_2O moieties ((Figure S7c).). Similar to the after OER sample, the C 1s spectrum of after MOR sample exhibits C=C, C–C, C–OH and COOH groups with the disappearance of keto group ((Figure S7d).). However, after MOR the intensity of aromatic C=C has been significantly reduced as compared to after OER which indicates that methanol oxidation causes more harm to the oxidized CNT.

Conclusion

In summary, we successfully synthesized the composite of Ni-doped Fe_2O_3 with oxidized CNT. The sheets of Ni-doped Fe_2O_3 are coupled with O–CNTs and thus formed a Mott-Schottky heterojunction to catalyze electrochemical water and methanol oxidation. Doping of Ni with Fe_2O_3 alters the g value and enhances the donor density, evidenced by EPR spectroscopy MS analysis and thus, improves the electrical conductivity. Ni–Fe_2O_3 further coupled with mildly oxidized CNT and improved the OER and MOR dramatically. The high OER activity, η_{10} of 310 mV is attributed to the larger electrochemical surface area, ECSA of 10.3 mF cm^{-2}. Furthermore, Ni–Fe_2O_3/O–CNT demonstrates j @ 10 mA cm^{-2} at the low potentials of 1.50 V and 1.46 V vs. RHE in 0.5 M and 1 M MeOH. Ni–Fe_2O_3/O–CNT show very good stability and durability both in presence and absence of methanol. The synergistic effect arises due to the development of hetero interfaces of Ni–Fe_2O_3 and O–CNT and hence, favors the electrocatalytic reactions. We believe our approach provides an effective way of fabrication efficient catalysts.

Experimental Section

Synthesis of Ni–Fe_2O_3/O–CNT: Firstly, we placed 150 mg of MWCNT in a mixture of 15 ml of conc. H_2SO_4 and 8 ml of 30% H_2O_2 in a 50 ml beaker and stirred for 8 h continuously using a magnetic stirrer. After collecting the product using filtration, we centrifuged several times with DI H_2O and ethanol. Then, we dried the residue

for 12 h in an oven at 80 °C. This product is termed as oxidized CNT (O–CNT).

In the next step, we added 100 mg of O–CNT into a homogeneous solution of 50 mM of $K_3[Fe(CN)_6]$ and 5 mM $Ni(NO_3)_2.6H_2O$ and sonicated for 30 minutes. Then we transferred the final mixture to a stainless-steel autoclave with a capacity of 50 mL, where the total homogenous mixture volume was 35 mL and we kept it in an electric oven at 180 ^{0}C for 12 h. After the natural cooling of the autoclave, we washed the product many times with DI water and ethanol and dried at 80 °C overnight. We called the final product as **Ni–Fe_2O_3/O–CNT**. In a similar way we prepared Fe_2O_3/O–CNT without the addition of Ni salt. To get Fe_2O_3, we did the hydrothermal treatment of $K_3[Fe(CN)_6]$ at 180 °C for 12 h. Finally, we characterized Ni–Fe_2O_3/O–CNT using XRD, XPS, TEM and Raman spectroscopy.

Acknowledgements

GDN, BM and SM are thankful to Israel Science Foundation and Israel Prime Ministry Office for partially carrying out this research under Israel National Research Center for Electrochemical Propulsion (INREP) Grant (No: ISF 2797/11). SM is grateful for the PBC Fellowship Program for Outstanding Chinese and Indian Post-doctoral Fellows – 2020/2021. RL and AP grateful acknowledge financial support from the Italian Ministry of University and Research (MIUR) through grant "Dipartimenti di Eccellenza-2017 Materials for Energy".

Conflict of Interest

The authors declare no conflict of interest.

Data Availability Statement

Research data are not shared.

Keywords: carbon nanotubes · electrochemistry · methanol oxidation reaction · Mott-Schottky catalysts · oxygen evolution reaction

[1] C. Spöri, P. Briois, H. N. Nong, T. Reier, A. Billard, S. Kühl, D. Teschner, P. Strasser, *ACS Catal.* **2019**, *9*, 6653–6663.
[2] B. Malik, S. Anantharaj, K. Karthick, D. K. Pattanayak, S. Kundu, *Catal. Sci. Technol.* **2017**, *7*, 2486–2497.
[3] Q. Wang, Z. Zhao, Y. Jia, M. Wang, W. Qi, Y. Pang, J. Yi, Y. Zhang, Z. Li, Z. Zhang, *ACS Appl. Mater. Interfaces* **2017**, *9*, 36817–36827.
[4] Y. Chen, K. Yang, B. Jiang, J. Li, M. Zeng, L. Fu, *J. Mater. Chem. A* **2017**, *5*, 8187–8208.
[5] S. Li, J. Yang, C. Song, Q. Zhu, D. Xiao, D. Ma, *Adv. Mater.* **2019**, *31*, 1–12.
[6] S. Kundu, B. Malik, D. K. Pattanayak, V. K. Ragupathy, P. Pillai, *ChemistrySelect* **2017**, *2*, 9943–9946.
[7] K. Patil, P. Babar, D. M. Lee, V. Karade, E. Jo, S. Korade, J. H. Kim, *Sustain. Energy Fuels* **2020**, *4*, 5254–5263.
[8] R. Michalsky, A. M. Avram, B. A. Peterson, P. H. Pfromm, A. A. Peterson, *Chem. Sci.* **2015**, *6*, 3965–3974.
[9] S. Kundu, B. Malik, A. Prabhakaran, D. K. Pattanayak, V. K. Pillai, *Chem. Commun.* **2017**, *53*, 9809–9812.
[10] S. Kundu, B. Malik, D. K. Pattanayak, V. K. Pillai, *ChemElectroChem* **2018**, *5*, 1670–1676.
[11] B. Malik, K. Vijaya Sankar, R. Konar, Y. Tsur, G. D. Nessim, *ChemElectroChem* **2020**, *8*, 517–523.
[12] S. K. T. Aziz, B. Malik, H. K. Sadhanala, A. Gedanken, M. Noked, G. D. Nessim, **2020**, *3*, 10914–10921.
[13] S. Kundu, B. Malik, D. K. Pattanayak, P. Ragupathy, V. K. Pillai, *ChemistrySelect* **2017**, *2*, 9943–9946.
[14] A. Zagalskaya, V. Alexandrov, *J. Phys. Chem. Lett.* **2020**, *11*, 2695–2700.
[15] S. Cherevko, T. Reier, A. R. Zeradjanin, Z. Pawolek, P. Strasser, K. J. J. Mayrhofer, *Electrochem. Commun.* **2014**, *48*, 81–85.
[16] K. A. Stoerzinger, O. Diaz-Morales, M. Kolb, R. R. Rao, R. Frydendal, L. Qiao, X. R. Wang, N. B. Halck, J. Rossmeisl, H. A. Hansen, T. Vegge, I. E. L. Stephens, M. T. M. Koper, Y. Shao-Horn, *ACS Energy Lett.* **2017**, *2*, 876–881.
[17] M. E. G. Lyons, S. Floquet, *Phys. Chem. Chem. Phys.* **2011**, *13*, 5314–5335.
[18] S. Shit, W. Jang, S. Bolar, N. C. Murmu, H. Koo, T. Kuila, *ACS Appl. Mater. Interfaces* **2019**, *10*, 27712–27722, https://doi.org/10.1021/acsami.9b06635.
[19] R. Gond, D. K. Singh, M. Eswaramoorthy, P. Barpanda, *Angew. Chem. Int. Ed.* **2019**, *58*, 8330–8335; *Angew. Chem.* **2019**, *131*, 8418–8423.
[20] D. Lim, S. Kim, N. Kim, E. Oh, S. E. Shim, S. H. Baeck, *ACS Sustainable Chem. Eng.* **2020**, *8*, 4431–4439.
[21] Y. Yang, L. Dang, M. J. Shearer, H. Sheng, W. Li, J. Chen, P. Xiao, Y. Zhang, R. J. Hamers, S. Jin, *Adv. Energy Mater.* **2018**, *8*, 1–9.
[22] M. Yu, G. Moon, E. Bill, H. Tüysüz, *ACS Appl. Energ. Mater.* **2019**, *2*, 1199–1209.
[23] W. Adamson, C. Jia, Y. Li, C. Zhao, *Electrochim. Acta* **2020**, *355*, 136801–136816.
[24] S. Gupta, A. Yadav, S. Bhartiya, M. K. Singh, A. Miotello, A. Sarkar, N. Patel, *Nanoscale* **2018**, *10*, 8806–8819.
[25] N. L. W. Septiani, Y. V. Kaneti, Y. Guo, B. Yuliarto, X. Jiang, Y. Ide, N. Nugraha, H. K. Dipojono, A. Yu, Y. Sugahara, D. Golberg, Y. Yamauchi, *ChemSusChem* **2020**, *13*, 1645–1655.
[26] M. A. Kazakova, D. M. Morales, C. Andronescu, K. Elumeeva, A. G. Selyutin, A. V. Ishchenko, G. V. Golubtsov, S. Dieckhöfer, W. Schuhmann, J. Masa, *Catal. Today* **2020**, *357*, 259–268, 0–1.
[27] Q. Zhou, T. T. Li, J. Qian, Y. Hu, F. Guo, Y. Q. Zheng, *J. Mater. Chem. A* **2018**, *6*, 14431–14439.
[28] A. Ramírez, P. Hillebrand, D. Stellmach, M. M. May, P. Bogdanoff, S. Fiechter, *J. Phys. Chem. C* **2014**, *118*, 14073–14081.
[29] R. Subbaraman, D. Tripkovic, K. C. Chang, D. Strmcnik, A. P. Paulikas, P. Hirunsit, M. Chan, J. Greeley, V. Stamenkovic, N. M. Markovic, *Nat. Mater.* **2012**, *11*, 550–557.
[30] D. M. Morales, M. A. Kazakova, S. Dieckhöfer, A. G. Selyutin, G. V. Golubtsov, W. Schuhmann, J. Masa, *Adv. Funct. Mater.* **2020**, *30*, 1–12.
[31] J. Li, Z. Luo, F. He, Y. Zuo, C. Zhang, J. Liu, X. Yu, R. Du, T. Zhang, M. F. Infante-Carrió, P. Tang, J. Arbiol, J. Llorca, A. Cabot, *J. Mater. Chem. A* **2018**, *6*, 22915–22924.
[32] S. Anantharaj, H. Sugime, S. Noda, *ACS Appl. Mater. Interfaces* **2020**, *12*, 27327–27338.
[33] U. B. Demirci, *J. Power Sources* **2007**, *169*, 239–246.
[34] B. Y. Xia, H. Bin Wu, X. Wang, X. W. Lou, *J. Am. Chem. Soc.* **2012**, *134*, 13934–13937.
[35] X. Yang, J. Xue, L. Feng, *Chem. Commun.* **2019**, *55*, 11247–11250.
[36] S. M. Alia, G. Zhang, D. Kisailus, D. Li, S. Gu, K. Jensen, Y. Yan, *Adv. Funct. Mater.* **2010**, *20*, 3742–3746.
[37] Z. A. C. Ramli, S. K. Kamarudin, *Nanoscale Res. Lett.* **2018**, *13*, https://doi.org/10.1186/s11671-018-2799-4.
[38] Z. Jusys, T. J. Schmidt, L. Dubau, K. Lasch, L. Jörissen, J. Garche, R. J. Behm, *J. Power Sources* **2002**, *105*, 297–304.
[39] R. Ganesan, J. S. Lee, *Angew. Chem. Int. Ed.* **2005**, *44*, 6557–6560; *Angew. Chem.* **2005**, *117*, 6715–6718.
[40] K. Xiang, D. Wu, X. Deng, M. Li, S. Chen, P. Hao, X. Guo, J. L. Luo, X. Z. Fu, *Adv. Funct. Mater.* **2020**, *30*, 1–10.
[41] B. Zhao, J. Liu, X. Wang, C. Xu, P. Sui, R. Feng, L. Wang, J. Zhang, J. L. Luo, X. Z. Fu, *Nano Energy* **2021**, *80*, 105530.
[42] Y. T. Liu, Q. B. Yuan, D. H. Duan, Z. L. Zhang, X. G. Hao, G. Q. Wei, S. Bin Liu, *J. Power Sources* **2013**, *243*, 622–629.
[43] K. Miyazaki, H. Ishihara, K. Matsuoka, Y. Iriyama, K. Kikuchi, Y. Uchimoto, T. Abe, Z. Ogumi, *Electrochim. Acta* **2007**, *52*, 3582–3587.
[44] Y. Yin, X. Zhang, C. Sun, *Prog. Nat. Sci.* **2018**, *28*, 430–436.
[45] A. Samanta, S. Das, S. Jana, *ACS Sustainable Chem. Eng.* **2019**, *7*, 12117–12124.

[46] L. Zhong, H. Zhou, R. Li, H. Cheng, S. Wang, B. Chen, Y. Zhuang, J. Chen, A. Yuan, *J. Colloid Interface Sci.* **2021**, *599*, 46–57.
[47] L. Zhong, H. Zhou, R. Li, T. Bian, S. Wang, A. Yuan, *J. Colloid Interface Sci.* **2021**, *584*, 439–448.
[48] J. Feng, H. Zhou, D. Chen, T. Bian, A. Yuan, *Electrochim. Acta* **2020**, *331*, 135445.
[49] X. Lu, W. L. Yim, B. H. R. Suryanto, C. Zhao, *J. Am. Chem. Soc.* **2015**, *137*, 2901–2907.
[50] G. Pezzotti, W. Zhu, *Phys. Chem. Chem. Phys.* **2015**, *17*, 2608–2627.
[51] V. Modafferi, C. Triolo, M. Fiore, A. Palella, L. Spadaro, N. Pianta, R. Ruffo, S. Patanè, S. Santangelo, M. G. Musolino, *Nanomaterials* **2020**, *10*, 1–18.
[52] I. Chamritski, G. Burns, *J. Phys. Chem. B* **2005**, *109*, 4965–4968.
[53] J. Wang, W. B. White, J. H. Adair, *J. Am. Ceram. Soc.* **2005**, *88*, 3449–3454.
[54] R. N. Bhowmik, A. Saravanan, *J. Appl. Phys.* **2010**, *107*, https://doi.org/10.1063/1.3327433.
[55] K. F. McCarty, *Solid State Commun.* **1988**, *68*, 799–802.
[56] R. D. Rodriguez, E. Sheremet, T. Deckert-Gaudig, C. Chaneac, M. Hietschold, V. Deckert, D. R. T. Zahn, *Nanoscale* **2015**, *7*, 9545–9551.
[57] C. P. Marshall, W. J. B. Dufresne, C. J. Rufledt, *J. Raman Spectrosc.* **2020**, *51*, 1522–1529.
[58] D. L. A. de Faria, F. N. Lopes, *Vib. Spectrosc.* **2007**, *45*, 117–121.
[59] M. S. Dresselhaus, G. Dresselhaus, R. Saito, A. Jorio, *Phys. Rep.* **2005**, *409*, 47–99.
[60] S. F. A. Kettle, E. Diana, E. M. C. Marchese, E. Boccaleri, P. L. Stanghellini, *J. Raman Spectrosc.* **2011**, *42*, 2006–2014.
[61] R. Reveendran, M. A. Khadar, *Mater. Chem. Phys.* **2018**, *219*, 142–154.
[62] A. A. Jahagirdar, N. Dhananjaya, D. L. Monika, C. R. Kesavulu, H. Nagabhushana, S. C. Sharma, B. M. Nagabhushana, C. Shivakumara, J. L. Rao, R. P. S. Chakradhar, *Spectrochim. Acta Part A* **2013**, *104*, 512–518.

Manuscript received: February 7, 2022
Revised manuscript received: April 4, 2022